



# A Highly Sensitive and Selective Laser-Based BTEX Sensor for Occupational and Environmental Monitoring

Mhanna Mhanna<sup>1</sup>, Mohamed Sy<sup>1</sup>, Ayman Arfaj<sup>2</sup>, Jose Llamas<sup>2</sup>, Aamir Farooq<sup>1</sup>

<sup>1</sup>Mechanical Engineering Program, Physical Science and Engineering Division, Clean Combustion Research Center, King Abdullah University of Science and Technology (KAUST), Thuwal 23955-6900, Saudi Arabia

<sup>2</sup>Saudi Aramco, Environmental Protection, 9f Al-Midra Tower, Dhahran 31311, Saudi Arabia

Correspondence to: Aamir Farooq (aamir.farooq@kaust.edu.sa)

**Abstract.** A mid-infrared laser-based sensor is designed and demonstrated for trace detection of benzene, toluene, ethylbenzene, and xylene isomers at ambient conditions. The sensor is based on a distributed feedback inter-band cascade laser emitting near 3.29  $\mu\text{m}$  and an off-axis cavity-enhanced absorption spectroscopy configuration with an optical gain of  $\sim 2800$ . Wavelength tuning and a deep neural networks (DNN) model were employed to enable simultaneous and selective BTEX measurements. The sensor performance was demonstrated by measuring BTEX mole fractions in various mixtures. At an integration time of 10 seconds, minimum detection limits of 11.4, 9.7, 9.1, 10, 15.6, and 12.9 ppb were achieved for benzene, toluene, ethylbenzene, m-xylene, o-xylene, and p-xylene, respectively. The sensor can be used to detect tiny BTEX leaks in petrochemical facilities and to monitor air quality in residential and industrial areas for workplace pollution.

## 1 Introduction

Human activity, especially transportation and industrial emissions, have deleterious impacts on air quality. Petrochemical industries are the major emitters of volatile organic compounds (VOCs) (Yassaa et al.; Zhang et al.). In particular, benzene, toluene, ethylbenzene and xylene isomers (BTEX) are emitted from engine exhausts, gasoline service stations, petrochemical refineries, and the paint and rubber industries (Foo). Indoor sources of BTEX include gas boilers (Helmer), oil stoves (Greenburg et al.), candles and cleaning products (Sekar et al.).

The ubiquity and adverse effects of these species, even at the parts per billion (ppb) level, on environmental and human health have attracted increasing attention. Studies have strongly linked global warming, stratospheric ozone depletion, and petrochemical smog to BTEX emissions (Sinha et al.). The carcinogenic and mutagenic effects of BTEX species on human health are recognized by the World Health Organization (WHO) (Organization) and US Environmental Protection Agency (EPA) (Williams et al.), and have raised tremendous concerns in recent years.

Exposure to high concentration of volatile organic compounds (VOCs) may cause acute symptoms such as irritations of the nose, throat, and eyes, in addition to causing headache, nausea, dizziness, and allergic skin reactions. Moreover, some components of VOCs such as BTEX can lead to chronic health risks. Benzene is a carcinogen, and toluene exposure can lead to devastating neurological disorders (Dorsey). Long-term exposure to xylene may cause headache, extreme tiredness, tremors,



impaired concentration, and short-term memory loss. If high concentrations of hydrocarbons replace oxygen in breath, it can sensitize the heart to stress hormones causing abnormal rhythms and ventricular fibrillation that can cause sudden death (Adgey et al.). A brief exposure (< 30 seconds) to high concentrations of BTEX (> 2%) and low-oxygen atmosphere can result in rapid onset of respiratory depression, hypoxia, and fatal cardiac arrhythmias (Miller and Mazur). Long-term BTEX exposure can have narcotic effects, causing dizziness, rapid disorientation, and confusion that can lead to loss of judgment, narcosis, and incapacitation (Sugie et al.).

A multitude of studies have proved a strong association between occupational exposure to benzene by inhalation and an increased incidence of certain types of leukemia. Adverse health effects of occupational benzene exposure include acute myelogenous leukemia, blood diseases, plastic anemia, injury of the immune system, and menstruation disorders (Esteve-Turrillas et al.). Occupational toluene exposure is associated with central nervous system depression, tiredness, dizziness, faintness, memory loss, nausea, appetite decrease, hearing loss, and unconsciousness. Acute occupational exposure to elevated levels of ethylbenzene may result in neurological effects such as light-headedness, dizziness and eye irritation. Chronic occupational exposure to xylene may affect the central nervous system, cause skin irritation, skin stimulation, dryness, skin rapture, blister and skin dermatitis (Bina et al.).

Reliable sensors are extremely important for these harmful pollutants (Mhanna et al., 2023). Most existing sensors are based on sample extraction and offline analysis in the laboratory. For instance, gas chromatography, mass spectrometry and Fourier transform infrared spectroscopy (FTIR) (Roubaud et al.; Gregory et al.) involve highly expensive and complex instrumentation, require trained analysts for operation and are not suitable for field application due to their size and weight. Flame- and photo- ionization detection (FID and PID) are commonly used for benzene measurement, but are affected by high humidity. In addition, these sensors are time consuming due to the intensive sample collection, transportation, and analysis steps, which leads to the loss of spatial and temporal resolution of the measurements.

In recent years, advanced laser sources have been developed, which possess narrow emission linewidths and broad frequency tuning that provide access to the absorption bands of various molecules. In addition, significant improvements have been achieved in the robustness, stability, power consumption and heat management of these lasers. These characteristics make spectroscopic absorption sensors simple and accurate, and thus open a new strategy in remote sensing of gases. The ultraviolet (UV) wavelength region is an attractive option for BTEX measurements. Tunnicliff et al. demonstrated the measurement of BTEX components based on absorption photometry in the UV range circa 1950 (Bui and Hauser). However, the broad absorption features of many other hydrocarbons in that range do not permit interference-free measurements. Alternatively, infrared (IR) absorption spectra of hydrocarbons provide the possibility of more selective sensing of gaseous species (Elkhazraji et al., 2023; Elkhazraji et al., 2022). Numerous sensors for hydrocarbons using the mid-IR range have appeared in literature, and some devices have been commercialized (Farooq et al.). Previously, Sydoryk et al. (Sydoryk et al.) developed a mid-IR laser-based sensor for BTX detection near 1038  $\text{cm}^{-1}$ . However, this region contains significant interference from ozone and ethylene, and even trace quantities of these interfering gases can result in large errors in the measured concentrations of BTEX.



65 The similar absorbance spectra of BTEX species in the IR are the main cause of the poor selectivity of existing sensors. In a previous work, we demonstrated selective BTEX sensing using deep neural networks (DNNs) to differentiate the similar absorbance spectra of BTEX molecules (Mhanna et al.). In this work, cavity-enhanced absorption spectroscopy (CEAS) coupled with an updated DNN model are used to achieve high sensitivity and selectivity for a miniaturized BTEX sensor for occupational/industrial hygiene and atmospheric monitoring.

## 70 2 Methodology

### 2.1 Beer-Lambert law

The principle of laser absorption spectroscopy relates the spectral absorbance to the gas properties via Beer-Lambert Law (Swinehart):

$$\alpha_{SP} = \sigma(\nu, T, P) \cdot n(T, P) \cdot L \cdot \chi \quad (1)$$

75 where  $\alpha_{SP}$  is the measured absorbance for a single pass of the laser,  $\sigma(\nu, T, P)$  is the temperature- and pressure-dependent absorption cross-section that describes species propensity to absorb light at a frequency  $\nu$ ,  $n$  is the total number density of the gas mixture,  $L$  is the physical absorption path-length, and  $\chi$  is the mole fraction of the absorbing species. At frequencies where multiple species absorb, a composite absorbance results from the summation of individual absorbances. For a given absorption cross-section and experimental conditions  $(T, P)$ , smaller values of mole fraction ( $\chi$ ) can only be measured by increasing the path-length, ( $L$ ). One effective methodology for increasing  $L$  utilizes two highly reflective parallel concave mirrors to create an optical cavity through multiple reflections of the laser light.

85 Cavity ringdown spectroscopy (CRDS) and cavity-enhanced absorption spectroscopy (CEAS) have been used for trace detection of gaseous species (Kosterev and Tittel). In CRDS, laser intensity accumulates inside the cavity and then its characteristic exponential decay time is measured, while in CEAS, the laser wavelength is typically tuned over a specific spectral range to record spectrally-resolved absorption features. The laser intensity is attenuated by absorbance of the target species and the characteristics of the cavity mirrors. The cavity absorbance,  $\alpha_{CEAS}$ , is related to an equivalent single-pass absorbance,  $\alpha_{SP}$ , via Eq. (2) (Nasir and Farooq):

$$\alpha_{SP} = -\ln\left(1 - \frac{e^{\alpha_{CEAS}-1}}{G}\right) \quad (2)$$

where  $\alpha_{CEAS}$  is measured from the transmitted ( $I_t$ ) and incident ( $I_0$ ) laser intensities using:

90 
$$\alpha_{CEAS} = -\ln\left(\frac{I_t}{I_0}\right) \quad (3)$$

and  $G$  is the cavity gain, which is related to the mirrors' reflectivity ( $R$ ) by:

$$G = \frac{R}{1-R} \quad (4)$$



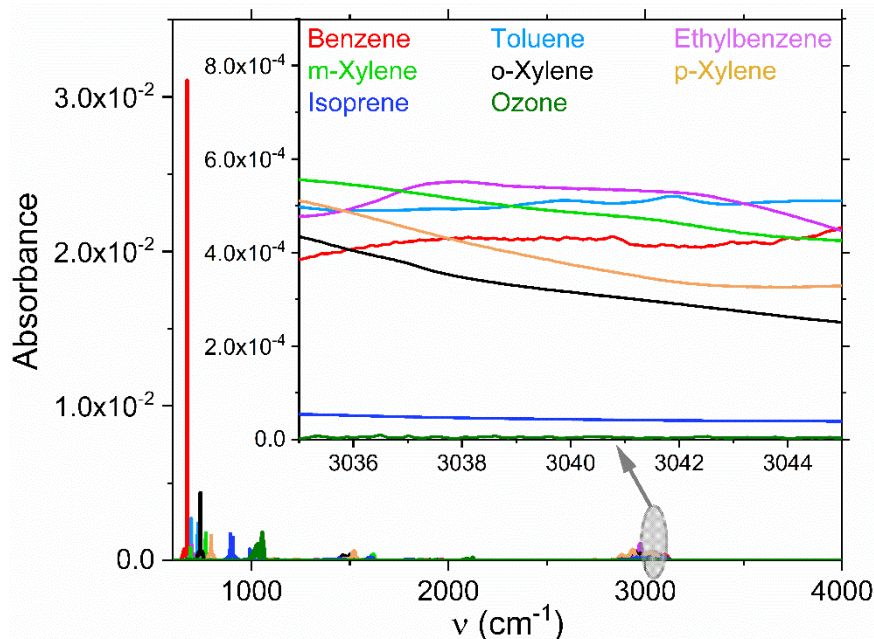
Here,  $\alpha_{SP}$  is calculated from Eq. (2) and then used in Beer-Lambert relation (1) to calculate the target species mole fraction.

By combining Eqs. (1) to (4) for the case of a weak absorber and high reflectivity ( $\alpha_{SP} \rightarrow 0$  and  $R \rightarrow 1$ ), and letting  $U =$   
 95  $1 - e^{-\alpha_{SP}}$ , we get:

$$\alpha_{CEAS} = G \cdot U \quad (5)$$

## 2.2 Wavelength selection

BTEX and many other hydrocarbons have broad absorbance spectra in the ultraviolet (UV) range, which obfuscates  
 interference-free and selective sensing. Alternatively, the infrared (IR) region provides opportunities for highly selective  
 100 detection of hydrocarbons and air pollutants. Based on the IR absorbance spectra of BTEX shown in Fig. 1, given in the Pacific  
 Northwest National Laboratory (PNNL) database (Sharpe et al.), the best frequency to measure BTEX is near  $700 \text{ cm}^{-1}$ .  
 However, this spectral region is currently not widely accessible by commercially available semiconductor lasers. Benzene  
 measurements near  $3090 \text{ cm}^{-1}$  (Sur et al.) and  $1040 \text{ cm}^{-1}$  (Lewicki et al.) suffer significant interference from isoprene and  
 ozone, respectively. Therefore, we selected the ro-vibrational band of BTEX near  $3040 \text{ cm}^{-1}$ , shown in the inset of Fig. 1,  
 105 which has negligible isoprene and ozone interference (Mhanna et al., 2022a). This region contains broad and overlapping  
 absorbance spectra of BTEX which make it challenging to separate the individual absorbance contributions. We note that the  
 selected region is insensitive to the presence of carbon dioxide, water vapor, acetone, ammonia, nitrous oxide, carbonyl sulfide,  
 formic acid, nitrogen dioxide and nitric acid (Sharpe et al.; Gordon et al.).



110 **Figure 1: BTEX spectra in the C-H stretching band. Spectral data taken from the PNNL database (Sharpe et al.) over  $600 - 4000 \text{ cm}^{-1}$  and simulated at  $T = 25 \text{ }^\circ\text{C}$ ,  $P = 1 \text{ atm}$ ,  $L = 30 \text{ cm}$ ,  $\chi = 1000 \text{ ppm}$ . The inset shows a close-up view over  $3035 - 3045 \text{ cm}^{-1}$ .**



## 2.3 Deep neural networks

Being inspired by the biological systems of neurons and synapses, artificial neural networks (ANNs) are supervised learning algorithms that mimic human brain (Ma et al.). ANN architecture is based on an input layer which handles the input tensor, hidden layers which contain neurons, followed by an output layer which handles the target tensor (Agatonovic-Kustrin and Beresford). Deeper architectures which comprise more than a single hidden layer are referred to as deep neural networks (DNNs). DNN models are typically developed using a fully connected multilayer perceptron (MLP) associated with a backpropagation algorithm (Hornik et al.; Nielsen). The back propagation of neural networks (BPNN) involves a feed forward stage to train the input tensor, followed by a calculation and backpropagation of the resulting error, and finally updating the weights in order to minimize the error (Werbos). A fixed learning rate and partial derivatives are used to prevent under/overfitting in back propagation (Guo et al.).

## 2.4 Sensor setup

A distributed feedback interband cascade laser (DFB-ICL, Nanoplus) was utilized to emit near  $3.29 \mu\text{m}$  with an output power  $\sim 2 \text{ mW}$ . Higher power commercial lasers are not available in this region. To facilitate the optical alignment, the ICL was co-aligned with a  $670 \text{ nm}$  red laser (Thorlabs). An optical cavity was formed utilizing two ZnSe mirrors of 99.97% nominal reflectivity (LohnStar Optics) in a  $5 \text{ cm}$  gas sampling cell with an off-axis alignment. This suppressed the spurious coupling noise significantly in comparison to an on-axis cavity. The laser wavelength was tuned over  $3039.25 - 3040.5 \text{ cm}^{-1}$  by a linear ramp of the laser injection current at  $1 \text{ kHz}$  scan rate. A  $7.62\text{-cm}$  Germanium Fabry-Pérot etalon was used to convert the scan time to frequency (wavenumbers). The transmitted laser intensity was collected via a focusing lens on to an AC-coupled, TE-cooled photodetector (Bandwidth of  $1.5 \text{ MHz}$ , Vigo Systems). Figure 2 shows the schematic of the sensor setup. All measurements were carried out at  $298 \text{ K}$  and  $1 \text{ atm}$ .

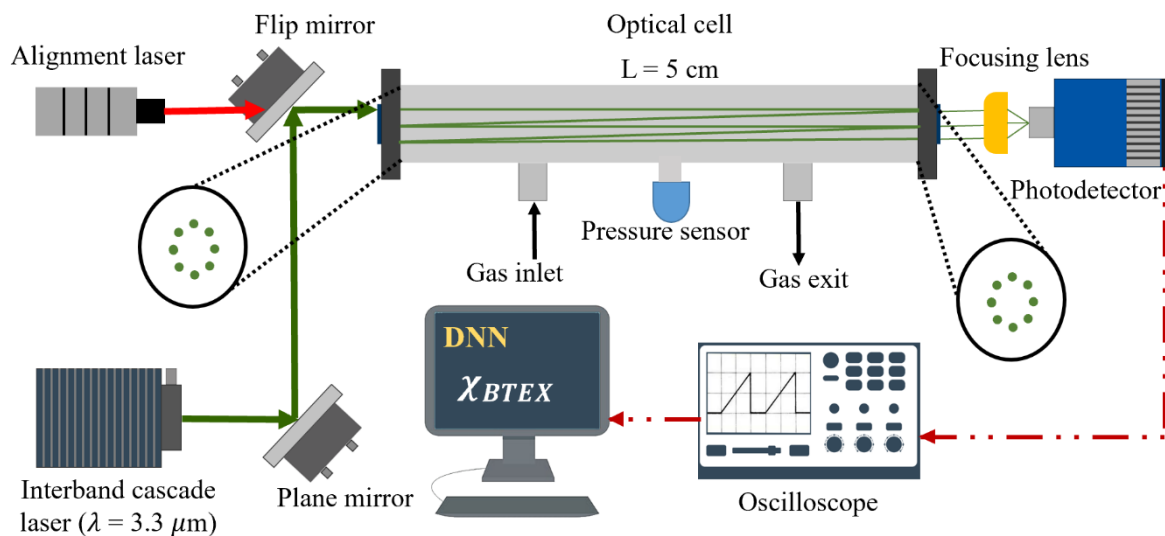


**Figure 2: Optical schematic of the sensor.**

### 135 3 Sensor calibration

#### 3.1 Allan variance

To characterize the long-term stability and obtain the optimum integration time of the sensor, Allan variance was calculated as follows (Giglio et al.):

$$s_x^2(t) = \frac{1}{K} \sum_{k=1}^{K-1} \frac{1}{2} (x_{k+1} - x_k)^2 \quad (6)$$

140 where  $K$  is the total number of data-points,  $x_k$  is the  $k$ th data-point averaged over an integration time  $t$ , and  $(x_{k+1} - x_k)$  is the difference between adjacent values of  $x_k$ . The Allan variance plot of the obtained absorbance signal of the sensor is shown in Fig. 3. The BTEX mixture contains 231, 379, 168, 182, 99, and 113 ppb of high-purity benzene (99.8%, Sigma-Aldrich), toluene (98%, VWR Chemicals), ethylbenzene (99.8%, Acros Organics), m-xylene, o-xylene, and p-xylene (99.8%, Acros Organics), respectively, diluted in nitrogen (99.999 %). Allan variance decreases at early times of the measurement due to the  
 145 domination of thermal noise until reaching its minimum value at around 10 seconds (Allan), and later increases due to laser intensity fluctuations (Giglio et al.).

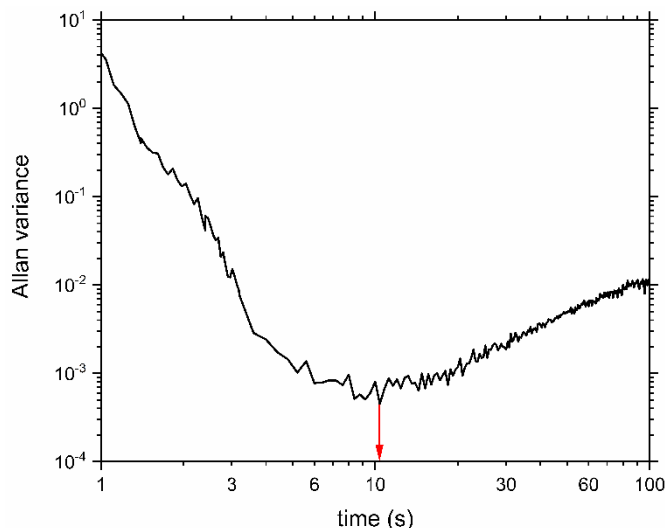


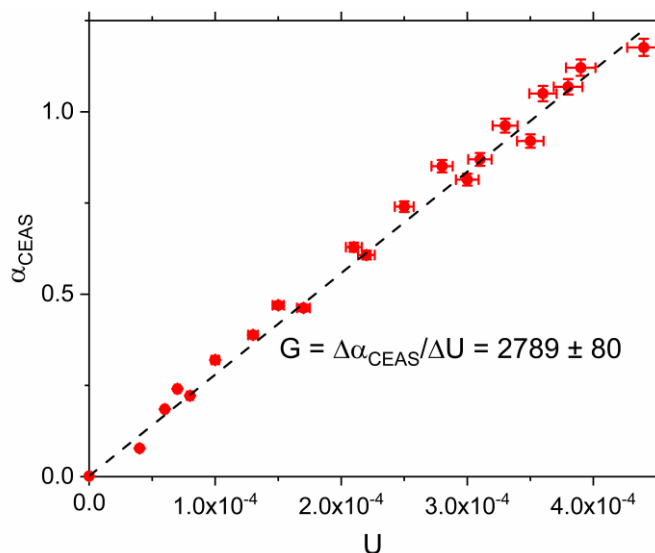
**Figure 3: Allan variance plot of the BTEX sensor. Optimal integration time is 10 seconds.**

### 3.2 Cavity gain evaluation

150 Cavity gain is determined by the mirrors' reflectivity, as shown in Eq. (4). Typically, significant deviation is observed between the actual and the manufacturer's nominal reflectivity specification, resulting in large uncertainty in the cavity gain. Thus, a more precise value of the cavity gain ( $G$ ) needs to be measured. We performed experiments for the evaluation of  $G$  using various mixtures of each BTEX species in nitrogen with known compositions (30 – 2000 ppb). Based on Eq. (5),  $G$  was determined by plotting  $\alpha_{CEAS}$  against  $U$ , as shown in Fig. 4. Here,  $G$  comes out to be  $2789 \pm 80$ , which translates into mirrors' reflectivity  $R = 99.964 \pm 0.001\%$ . The gain uncertainty ( $\pm 80$ ) was determined based on a 95% confidence interval of the measured values. This value of cavity gain increases the effective laser path-length from 5 cm (physical length of the gas sampling cell) to 139 m. All measurements reported here were carried out at ambient conditions with temperature and pressure uncertainties of 0.03% and 0.12% of the readings, respectively. Absorption cross-sections are reported to have 1.66% uncertainty (Sharpe et al.) and the physical path-length is known with an uncertainty of  $< 1\%$ . Uncertainties of  $\alpha_{CEAS}$  and  $U$  are calculated using the following two equations and come out to be 2.1% and 2.9%, respectively.

$$\frac{\partial \alpha_{CEAS}}{\alpha_{CEAS}} = \left[ \left( \frac{\partial I_0}{I_0} \right)^2 + \left( \frac{\partial I_t}{I_t} \right)^2 \right]^{\frac{1}{2}} \quad (7)$$

$$\frac{\partial U}{U} = \left[ \left( \frac{\partial \sigma}{\sigma} \right)^2 + \left( \frac{\partial P}{P} \right)^2 + \left( \frac{\partial \chi}{\chi} \right)^2 + \left( \frac{\partial T}{T} \right)^2 + \left( \frac{\partial L}{L} \right)^2 \right]^{\frac{1}{2}} \quad (8)$$



165 **Figure 4: Cavity absorbance as a function of  $U$  (see Eq. 5). The slope represents the cavity gain. Measurements were carried out over  $T = 298$  K and  $P = 1$  atm. BTEX mole fractions were varied over 30 – 2000 ppb.**

### 3.3 Free spectral range

The laser spot size ( $s$ ) in the cavity for laser wavelength  $\lambda$  of  $3.29 \mu\text{m}$ , mirrors' radius of curvature  $R_m$  of 1 m, and physical pathlength  $L$  of 5 cm was calculated to be 1.89 mm following the procedure described in our previous work (Mhanna et al., 2020). The rotation of the spots on the mirror surface after one round trip is an angle  $\theta$  given by:

170 
$$\theta = \cos^{-1}\left(1 - \frac{L}{R_m}\right) = 31^\circ \quad (9)$$

Thus, at least 11 non-overlapping spots would be formed on the mirrors. Although the cavity mirrors had a diameter of 25.4 mm, the exposed diameter of the mirrors was limited to about 8 mm due to the geometry of the mirror mounts. Therefore, the Lissajous circular spot pattern was aligned within a diameter of about 7 mm to avoid the light clipping near the edges of the mounts. This resulted in a circumference of about 22 mm which fits about 11 non-overlapping laser spots, and thus agrees with the spot rotation calculations.

175

The effective free spectral range ( $FSR_{eff}$ ) is calculated via Eq. (10) (Sayres et al.):

$$FSR_{eff} = \frac{c}{2nL} \quad (10)$$

where  $c$  is the speed of light in air,  $n$  is the number of non-overlapping spots, and  $L$  is the physical length of the optical cell. Due to the 11 non-overlapping spots,  $FSR_{eff}$  was reduced from 3000 MHz in an on-axis alignment to 273 MHz in the off-axis alignment, which significantly suppressed the cavity coupling noise by increasing the density of the cavity mode (Engel et al.).

180



## 4 Sensor performance

### 4.1 DNN prediction model

Python 3.8 software was utilized to build the deep neural network (DNN) model, which was shown in a previous work (Mhanna et al.) to outperform other prediction models in such classification applications due to its flexibility of tuning hyper-parameters.

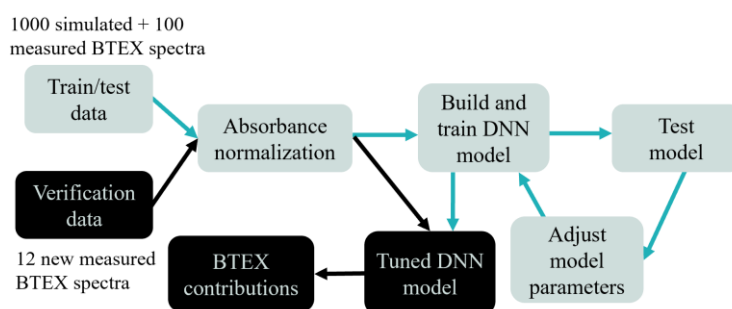
185 The model input is the composite BTEX absorbance spectra and the output is the individual BTEX contributions to the composite absorbance. A total of 1000 simulated and 100 measured BTEX absorbance spectra were utilized over the frequency range of 3039.25-3040.5 cm<sup>-1</sup>. Simulated spectra were generated using Eq. (11):

$$A = \sum_1^4 a_k * A_k \quad (11)$$

where  $A$  is the composite absorption spectrum,  $a_k$  is the individual contribution of species  $k$ , and  $A_k$  is the reference absorption spectrum of species  $k$  (Sharpe et al.). To highlight the weak absorbance features of BTEX species, a min-max normalization is applied to scale the data:

$$A_{normalized} = \frac{A - A_{min}}{A_{max} - A_{min}} \quad (12)$$

where  $A_{normalized}$  is the normalized absorbance, and  $A_{max}$  and  $A_{min}$  are the maximum and minimum absorbance values in  $A$ , respectively. Normalized absorbance is fed to the DNN model, where the input tensor consists of the 1100 scaled spectra, and the target tensor is the contribution of each BTEX species to the composite absorbance. The data are randomly split into 80/20 train/test datasets. A random search algorithm (RandomSearchCV) was applied to tune the hyper-parameters, including the number of nodes and hidden layers, activation functions, dropout layer, weight regularization, learning rate, momentum, number of epochs and batch size. The DNN model was optimized based on lowest root-mean-squared-error (RMSE), resulting in four hidden layers with 132, 64, 32, and 16 nodes, respectively. ReLU and Adamax (learning rate = 0.001 and momentum = 0.9) were opted as the activation function and optimizer, respectively. The model was run on 2000 epochs with a batch size of 64, and the validation loss was monitored with a patience of 20 epochs to avoid overfitting. The algorithm flowchart is shown in Fig. 5.



205 **Figure 5: Schematic for the overall process to build the DNN model and to extract BTEX contributions. Blue arrows correspond to model tuning using the 1000 simulated and 100 measured spectra, while black arrows correspond to extracting BTEX coefficients from the 12 separately measured spectra.**



## 4.2 Sensor validation

Gas samples containing BTEX species were manometrically prepared and DNN was applied to obtain the mole fractions of target species from the composite measured absorbance spectra. In these mixtures, the mole fraction of each BTEX species was varied over 0 – 2000 ppb, and measurements were carried out in two optical cells of 50 cm and 5 cm optical lengths. As a representative case, Figure 6 shows the measured absorbance spectrum of a mixture containing 121, 278, 422, 0, 151, and 775 ppm of benzene, toluene, ethylbenzene, m-xylene, o-xylene, and p-xylene, respectively. The tuned DNN model was utilized to predict the absorbance contributions, and the determined mole fractions came out to be 132, 261, 419, 6, 160, and 780 ppm of the target species, respectively. The predicted mole fractions were multiplied by the reference absorbance spectra from PNNL (Sharpe et al., 2004) to obtain the individual absorbance spectra of BTEX species shown in Fig. 6. These were added to reproduce the composite absorbance spectrum (dashed line), which turned out to be in good agreement with the measured spectrum (solid line), as shown in Fig. 6.

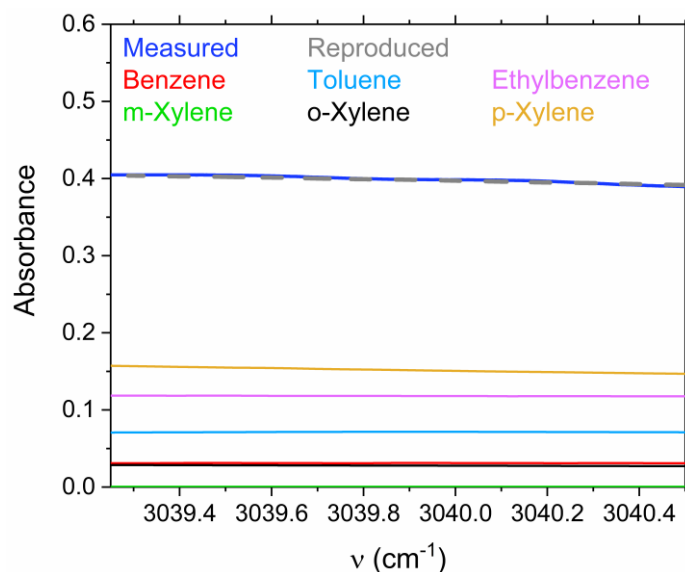
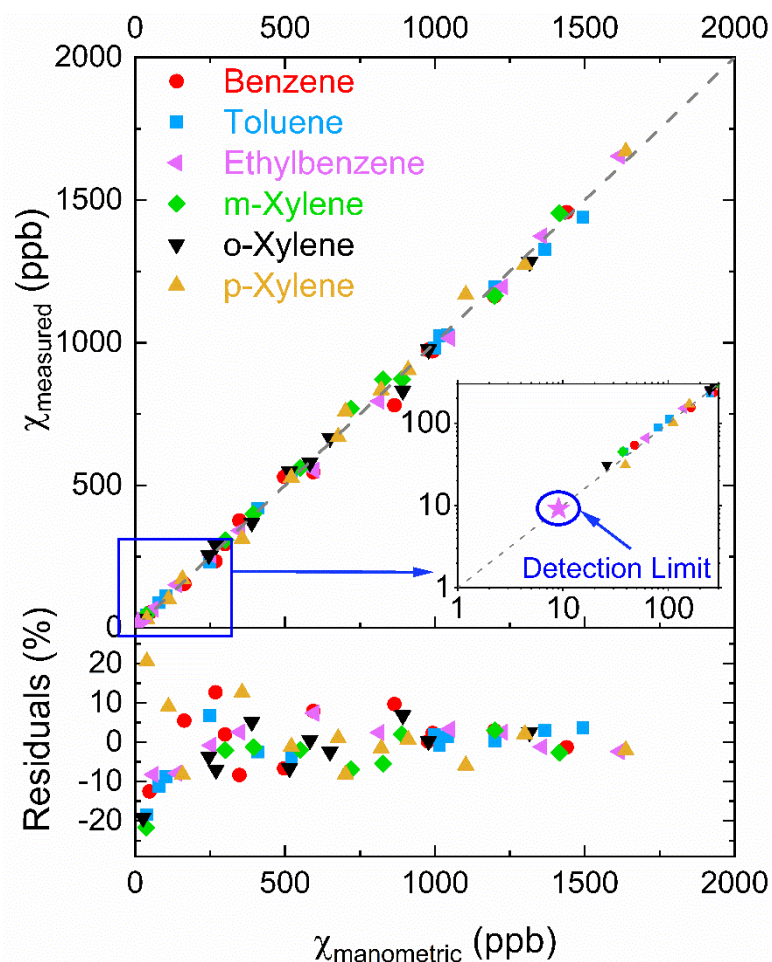


**Figure 6: Measured and reproduced absorbance spectra of a mixture containing 121, 278, 422, 0, 151, and 775 ppm of benzene, toluene, ethylbenzene, m-xylene, o-xylene, and p-xylene, respectively. The individual absorbance spectra were determined by multiplying the predicted mole fractions by the reference absorbance spectra from PNNL (Sharpe et al., 2004).**

Figure 7 plots experimentally determined mole fractions of BTEX against manometric (known) values. The dotted line represents the linear fit, which demonstrates remarkable agreement between the measured and manometric mole fractions. The residuals of these concentrations are shown in the bottom panel of Fig. 7. For all species, the residual is within 10% of the reading, which is in good agreement with the uncertainty of the measurements calculated using Eq. (5). The higher residual at low mole fractions (< 300 ppb) is due to the multi-fold dilution process used for preparing the mixtures to reach such low mole fraction values.



230 **Figure 7: Comparison of experimentally-measured and manometric mole fractions of BTEX species at ambient conditions. The dashed line represents the linear fit. The bottom panel shows the residuals between the measured and manometric mole fractions.**

### 4.3 Minimum detection limit

The minimum detection limit (MDL) is one of the most important parameters in ultra-sensitive sensors (Tittel et al.). While this can be obtained from the Allan variance of the absorbance signal, a more reasonable approach is to determine it from the signal-to-noise-ratio (SNR) of the measured signal, corresponding to an SNR = 1. Signal noise is reflected as fluctuations of the detected signal, which arise from various sources, such as thermal noise of the detector, laser intensity fluctuation, mechanical oscillations of the sensor components, and optical interference/reflection from the mirrors/lenses. The latter is the dominant noise factor in the case of multi-reflection schemes used for high sensitivity. Figure 8 shows two incident laser intensities through a non-absorbing (vacuum) medium. Ideally, both signals should perfectly overlap, resulting in an absorbance value of zero. However, due to signal fluctuations/noise, a minimum measurable absorbance was determined to be

235



240 ~ 0.1%, which corresponds to an SNR of 1. Equation 2 is then used to convert this absorption to minimum detection limits of 11.4, 9.7, 9.1, 10, 15.6, and 12.9 ppb for benzene, toluene, ethylbenzene, m-xylene, o-xylene, and p-xylene, respectively.

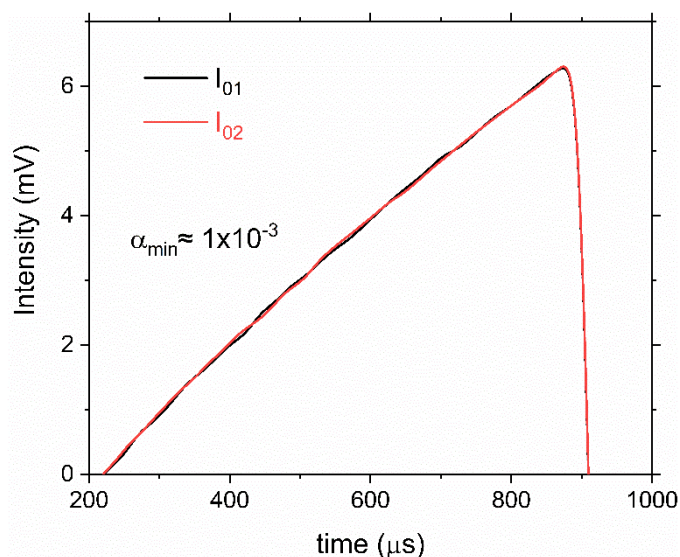


**Figure 8: Two representative incident laser intensity signals ( $I_0$ ) showing the fluctuations in these signals.**

## 5 Conclusions

245 A laser sensor based on cavity enhanced absorption spectroscopy has been demonstrated to measure trace concentrations of BTEX species. The single-pass absorption increased by more than three orders of magnitude due to the high reflectivity of the mirrors, thus enabling BTEX detection down to 9.1 ppb. This detection limit is obtained at an optimum integration time of 10 seconds. Wavelength tuning and deep neural networks were utilized to enable simultaneous and selective BTEX measurements. The sensor performance was validated with manometrically prepared BTEX mixtures. The sensor can be  
250 applied to monitor air quality in petrochemical facilities where the emissions of these species are likely, and near residential and industrial areas to monitor occupational/industrial hygiene and air pollution.

*Code availability.* Code can be provided on request.

255 *Data availability.* Data can be provided on request.

*Author contributions.* MM wrote the manuscript, developed the codes, prepared the experimental setup, ran experiments, and processed the data. MS helped in running the experiments and developing the models. AA and JL helped with the initial concept/design of the sensor. AF supervised the project. All authors reviewed the manuscript.

260



*Competing interests.* The contact author has declared that neither they nor their co-authors have any competing interests.

265 *Acknowledgements.* This work was funded by the Environmental Protection Department (EPD) of Saudi Aramco (RGC/3/4749-01).

## References

- Adgey, A. J., Johnston, P. W., and McMechan, S.: Sudden cardiac death and substance abuse, *Resuscitation*, 29, 219-221, 1995.
- 270 Agatonovic-Kustrin, S. and Beresford, R.: Basic concepts of artificial neural network (ANN) modeling and its application in pharmaceutical research, *Journal of pharmaceutical and biomedical analysis*, 22, 717-727, 2000.
- Allan, D. W.: Statistics of atomic frequency standards, *Proceedings of the IEEE*, 54, 221-230, 1966.
- Bina, B., Amin, M. M., Rashidi, A., and Pourzamani, H.: Benzene and toluene removal by carbon nanotubes from aqueous solution, *Archives of Environmental Protection*, 2012.
- 275 Bui, D. A. and Hauser, P. C.: A deep-UV light-emitting diode-based absorption detector for benzene, toluene, ethylbenzene, and the xylene compounds, *Sensors and Actuators B: Chemical*, 235, 622-626, 2016.
- Dorsey, A.: Toxicological profile for toluene, The Agency2000.
- Elkhazraji, A., Shakfa, M. K., Abualsaud, N., Mhanna, M., Sy, M., Marangoni, M., and Farooq, A.: Laser-based sensing in the long-wavelength mid-infrared: chemical kinetics and environmental monitoring applications, *Appl. Opt.*, 62, A46-A58, 10.1364/AO.481281, 2023.
- 280 Elkhazraji, A., Adil, M., Mhanna, M., Abualsaud, N., Alsulami, A. A., Shakfa, M. K., Marangoni, M., Giri, B., and Farooq, A.: A mid-IR laser diagnostic for HCN detection, *Proceedings of the Combustion Institute*, 2022.
- Engel, G. S., Drisdell, W. S., Keutsch, F. N., Moyer, E. J., and Anderson, J. G.: Ultrasensitive near-infrared integrated cavity output spectroscopy technique for detection of CO at 1.57  $\mu\text{m}$ : new sensitivity limits for absorption measurements in passive optical cavities, *Applied optics*, 45, 9221-9229, 2006.
- 285 Esteve-Turrillas, F. A., Pastor, A., and de la Guardia, M.: Assessing air quality inside vehicles and at filling stations by monitoring benzene, toluene, ethylbenzene and xylenes with the use of semipermeable devices, *Analytica Chimica Acta*, 593, 108-116, 2007.
- Farooq, A., Alquaity, A. B., Raza, M., Nasir, E. F., Yao, S., and Ren, W.: Laser sensors for energy systems and process industries: Perspectives and directions, *Progress in Energy and Combustion Science*, 91, 100997, 2022.
- 290 Foo, S.-C.: Benzene pollution from gasoline usage, *Science of the total environment*, 103, 19-26, 1991.
- Giglio, M., Patimisco, P., Sampaolo, A., Scamarcio, G., Tittel, F. K., and Spagnolo, V.: Allan deviation plot as a tool for quartz-enhanced photoacoustic sensors noise analysis, *IEEE transactions on ultrasonics, ferroelectrics, and frequency control*, 63, 555-560, 2015.
- 295 Gordon, I. E., Rothman, L. S., Hill, C., Kochanov, R. V., Tan, Y., Bernath, P. F., Birk, M., Boudon, V., Campargue, A., and Chance, K.: The HITRAN2016 molecular spectroscopic database, *Journal of Quantitative Spectroscopy and Radiative Transfer*, 203, 3-69, 2017.
- Greenburg, L., Eayers, M. R., Goldwater, L., and Smith, A. R.: Benzene (benzol) poisoning in the rotogravure printing industry in New York City, *Journal of Industrial Hygiene and Toxicology*, 21, 395-420, 1939.
- 300 Gregory, D., Jackson, R., and Bennett, P.: Mechanisms for the formation of exhaust hydrocarbons in a single cylinder spark-ignition engine, fueled with deuterium-labeled ortho-, meta- and para-xylene, *Combustion and flame*, 118, 459-468, 1999.
- Guo, H., Nguyen, H., Bui, X.-N., and Armaghani, D. J.: A new technique to predict fly-rock in bench blasting based on an ensemble of support vector regression and GLMNET, *Engineering with Computers*, 37, 421-435, 2021.
- 305 Helmer, K. J.: Accumulated Cases of Chronic Benzene Poisoning in the Rubber Industry, *Acta Medica Scandinavica*, 118, 354-375, 1944.



- Hornik, K., Stinchcombe, M., and White, H.: Multilayer feedforward networks are universal approximators, *Neural networks*, 2, 359-366, 1989.
- Kosterev, A. A. and Tittel, F. K.: Chemical sensors based on quantum cascade lasers, *IEEE journal of quantum electronics*, 38, 582-591, 2002.
- 310 Lewicki, R., Witinski, M., Li, B., and Wysocki, G.: Spectroscopic benzene detection using a broadband monolithic DFB-QCL array, *Novel In-Plane Semiconductor Lasers XV*, 241-247,
- Ma, J., Yu, Z., Qu, Y., Xu, J., and Cao, Y.: Application of the XGBoost machine learning method in PM<sub>2.5</sub> prediction: A case study of Shanghai, *Aerosol and Air Quality Research*, 20, 128-138, 2020.
- 315 Mhanna, M., Sy, M., and Farooq, A.: A selective laser-based sensor for fugitive methane emissions, *Scientific Reports*, 13, 1573, 2023.
- Mhanna, M., Sy, M., Elkhazraji, A., and Farooq, A.: Deep neural networks for simultaneous BTEX sensing at high temperatures, *Optics Express*, 30, 38550-38563, 2022a.
- Mhanna, M., Zhang, G., Kunnummal, N., and Farooq, A.: Cavity-enhanced measurements of benzene for environmental monitoring, *IEEE Sensors Journal*, 21, 3849-3859, 2020.
- 320 Mhanna, M., Sy, M., Arfaj, A., Llamas, J., and Farooq, A.: Laser-based selective BTEX sensing using deep neural networks, *Opt. Lett.*, 47, 3247-3250, 2022b.
- MILLER, T. M. and MAZUR, P. O.: Oxygen deficiency hazards associated with liquefied gas systems: Derivation of a program of controls, *American Industrial Hygiene Association Journal*, 45, 293-298, 1984.
- Nasir, E. F. and Farooq, A.: Intra-pulse laser absorption sensor with cavity enhancement for oxidation experiments in a rapid compression machine, *Optics express*, 26, 14601-14609, 2018.
- 325 Nielsen, M. A.: *Neural networks and deep learning*, Determination press San Francisco, CA, USA2015.
- Organization, W. H.: Exposure to cadmium: a major public health concern, *World Health Organization* <http://www.who.int/ipcs/features/cadmium.pdf>, 2010.
- 330 Roubaud, A., Minetti, R., and Sochet, L.: Oxidation and combustion of low alkylbenzenes at high pressure: comparative reactivity and auto-ignition, *Combustion and Flame*, 121, 535-541, 2000.
- Sayres, D. S., Moyer, E., Hanisco, T., St. Clair, J., Keutsch, F., O'Brien, A., Allen, N., Lapson, L., Demusz, J., and Rivero, M.: A new cavity based absorption instrument for detection of water isotopologues in the upper troposphere and lower stratosphere, *Review of Scientific Instruments*, 80, 044102, 2009.
- 335 Sekar, A., Varghese, G. K., and Varma, M. R.: Analysis of benzene air quality standards, monitoring methods and concentrations in indoor and outdoor environment, *Heliyon*, 5, e02918, 2019.
- Sharpe, S. W., Johnson, T. J., Sams, R. L., Chu, P. M., Rhoderick, G. C., and Johnson, P. A.: Gas-phase databases for quantitative infrared spectroscopy, *Appl. Spectrosc.*, 58, 1452-1461, 2004.
- 340 Sinha, S. N., Kulkarni, P., Shah, S., Desai, N., Patel, G., Mansuri, M., and Saiyed, H.: Environmental monitoring of benzene and toluene produced in indoor air due to combustion of solid biomass fuels, *Science of the total environment*, 357, 280-287, 2006.
- Sugie, H., Sasaki, C., Hashimoto, C., Takeshita, H., Nagai, T., Nakamura, S., Furukawa, M., Nishikawa, T., and Kurihara, K.: Three cases of sudden death due to butane or propane gas inhalation: analysis of tissues for gas components, *Forensic Science International*, 143, 211-214, 2004.
- 345 Sur, R., Ding, Y., Jackson, R., and Hanson, R.: Tunable laser-based detection of benzene using spectrally narrow absorption features, *Applied Physics B*, 125, 1-8, 2019.
- Swinehart, D. F.: The beer-lambert law, *Journal of chemical education*, 39, 333, 1962.
- Sydoryk, I., Lim, A., Jäger, W., Tulip, J., and Parsons, M. T.: Detection of benzene and toluene gases using a midinfrared continuous-wave external cavity quantum cascade laser at atmospheric pressure, *Applied optics*, 49, 945-949, 2010.
- 350 Tittel, F. K., Richter, D., and Fried, A.: Mid-infrared laser applications in spectroscopy, in: *Solid-state mid-infrared laser sources*, Springer, 458-529, 2003.
- Werbos, P. J.: *The roots of backpropagation: from ordered derivatives to neural networks and political forecasting*, John Wiley & Sons1994.
- Williams, R., Kaufman, A., and Garvey, S.: Next generation air monitoring (NGAM) VOC sensor evaluation report, EPA: Washington, DC, USA, 2015.



- 355 Yassaa, N., Brancaleoni, E., Frattoni, M., and Ciccioli, P.: Isomeric analysis of BTEXs in the atmosphere using  $\beta$ -cyclodextrin capillary chromatography coupled with thermal desorption and mass spectrometry, *Chemosphere*, 63, 502-508, 2006.
- Zhang, Y., Mu, Y., Liu, J., and Mellouki, A.: Levels, sources and health risks of carbonyls and BTEX in the ambient air of Beijing, China, *Journal of Environmental Sciences*, 24, 124-130, 2012.